Available online at www.sciencedirect.com
ScienceDirect
Journal of the European Ceramic Society 31 (2011) 29–41
www.elsevier.com/locate/jeurceramsoc

Calcium phosphate grafts produced by rapid prototyping based on laser cladding

R. Comesaña [a], F. Lusquiños [a], J. del Val [a], T. Malot [b], M. López-Álvarez [a], A. Riveiro [a], F. Quintero [a], M. Boutinguiza [a], P. Aubry [b], A. De Carlos [c], J. Pou [a,*]

[a] *Applied Physics Dpt., Universidade de Vigo, E.T.S.I.I., Lagoas-Marcosende, E-36310, Vigo, Spain*
[b] *ERDT/STAMP, Arts et Métiers Paris Tech, 151 Bd de l'Hôpital, 75013, Paris, France*
[c] *Biochemistry, Genetics and Immunology Dpt., Universidade de Vigo, Facultad de Biología, Lagoas-Marcosende, E-36310, Vigo, Spain*

Received 29 April 2010; received in revised form 2 August 2010; accepted 7 August 2010
Available online 17 September 2010

Abstract

Rapid prototyping based on laser cladding by powder injection has been used to produce calcium phosphate three-dimensional grafts without using molds. Precursor material comprising of hydroxyapatite (HA) powder was irradiated by means of an infrared Nd:YAG laser. The processing parameters and the thermal history of the processed material have been assessed and the process has been optimized to obtain solid parts. Processing by laser cladding lead to complete dehydroxylation of the precursor HA, the obtained microstructure is composed by an alpha-tricalcium phosphate (α-TCP) matrix with nucleated tetracalcium phosphate (TTCP) grains, in coexistence with oxyapatite and amorphous calcium phosphate. The produced bioceramic grafts were observed to be bioactive, leading to calcium-deficient hydroxyapatite precipitation and promoting pre-osteoblastic cell attachment and proliferation during "*in vitro*" cell culture test.

Keywords: Microstructure-final; Hydroxyapatite; Rapid prototyping; Laser processing; Biomedical applications

1. Introduction

A common challenge in regenerative medicine is the repair of bone defects produced by severe trauma, tumour resection or congenital deformity. When the defect is relatively large and self-healing is not produced by the body, the so called critical-size defect requires bone graft material addition to complete osseous reconstruction. Autogenous bone grafts have been considered as the first option, harvested bone from the same patient (typically from the iliac crest) is utilized to fill the defect, reducing the possibilities of graft rejection. From the point of view of the bone defect treatment, autografts are the best selection. Nevertheless, from the point of view of the patient overall well-being, the serious drawbacks of this approach include the induced additional pain in the harvest site, increment of the rehabilitation time and risk of post-operative complications. And, furthermore, harvest site morbidity seriously affects the patient normal life at long term and can derive in chronic donor site pain.[1,2] In addition, synthetic material is often required in combination with the autograft for large defects. Consequently, much effort has been directed to investigate about synthetic bone grafts and synthetic growth factors, being the objective a material capable to mimic the properties of bone.

Calcium phosphates have been tested as bone substitutes since several decades ago, due to their intrinsic properties that stimulate bone regeneration. Hydroxyapatite (HA), tricalcium phosphate (beta-TCP and alpha-TCP), tetracalcium phosphate (TTCP) or biphasic calcium phosphate as BCP (20% HA, 80% β-TCP) have been used as bone graft materials for orthopedic and maxillofacial surgery.[3–5] In low load bearing applications, such as cranial defect restoration, calcium phosphate bioceramics promote new bone growth and implant integration in the body. The use of calcium phosphate granules as graft for complex shaped defects has some difficulties, such as placing the material and keeping it within the desired geometry, moreover, migration of the particles is frequently produced.[6] However, calcium phosphate processing to produce a complex shape part is a costly and delicate task. In this sense, a technique to produce

* Corresponding author. Tel.: +34 986 812 216; fax: +34 986 812 201.
E-mail address: jpou@uvigo.es (J. Pou).

0955-2219/$ – see front matter © 2010 Elsevier Ltd. All rights reserved.
doi:10.1016/j.jeurceramsoc.2010.08.011

bioactive ceramic implants tailored to the patient anatomical needs would be helpful in the overall defect restoration process. Cranial defect restoration can be produced by a multi-step process involving the geometrical analysis of the required implant, with aid of three-dimensional computer tomography or magnetic resonance techniques.[7–9] The implant geometry is designed from these data and is translated into information suitable to the rapid prototyping working station; a patient tailored implant is obtained in this way. Different rapid prototyping techniques have been applied to implant production, such as stereolithography, laminated object manufacturing, three-dimensional printing and selective laser sintering.[10–15] Nevertheless, many of these techniques are limited to polymeric materials or require several post-processing steps to produce ceramic material parts. Selective laser sintering technique has been applied to mixtures of HA and biodegradable polymers, such process leads to HA particle entrapment in the sintered polymer.[16,17]

Rapid prototyping based on laser cladding is an alternative technique for production of real functional parts from an electronic drawing of the part. This technique utilizes a laser as energy source to stack successive layers of a desired material following the pattern given by the layered electronic design. The precursor material is feed in the form of powder which is injected into the laser focal spot and subsequently molten and solidified. Instead of just sintering the forming particles as in selective laser sintering, laser cladding produces much stronger parts by complete melting of the precursor particles.[18] Regarding bioceramics, laser cladding has already been applied to produce calcium phosphate coatings[19–25] and bioactive glass coatings[26] but not for production of three-dimensional bioceramic parts. Due to high temperature processing by this technique, the obtained material structure is modified in comparison with the precursor material, and different calcium phosphate phases are formed.[19,24] As a consequence, in-depth characterization of the processed material becomes important to determine its performance as biomaterial.

The aim of this work is demonstrate the ability of the rapid prototyping technique based on laser cladding for the production of three-dimensional calcium phosphate bioceramic grafts.

2. Materials and methods

2.1. Materials

The powder used as precursor material was CAPTAL 90 type calcium hydroxyapatite from Plasma-Biotal UK (some physic properties relevant for the laser cladding process are collected in Table 1). The hydroxyapatite crystallinity as evaluated by XRD was above 97.5%. Ti6Al4V plates with a thickness of 3 mm and dimensions of $100 \times 150\,mm^2$ were used as base material to grow up the CaP structures.

Table 1
HA precursor powder size and density.

	CAPTAL 90
Size d[90] (μm)	120
Bulk density (g/cm^3)	1.1
Thermal conductivity at 25 °C (W/mK)	1.0
Coefficient of thermal expansion 0–1000 °C (10^{-6} K^{-1})	14.8

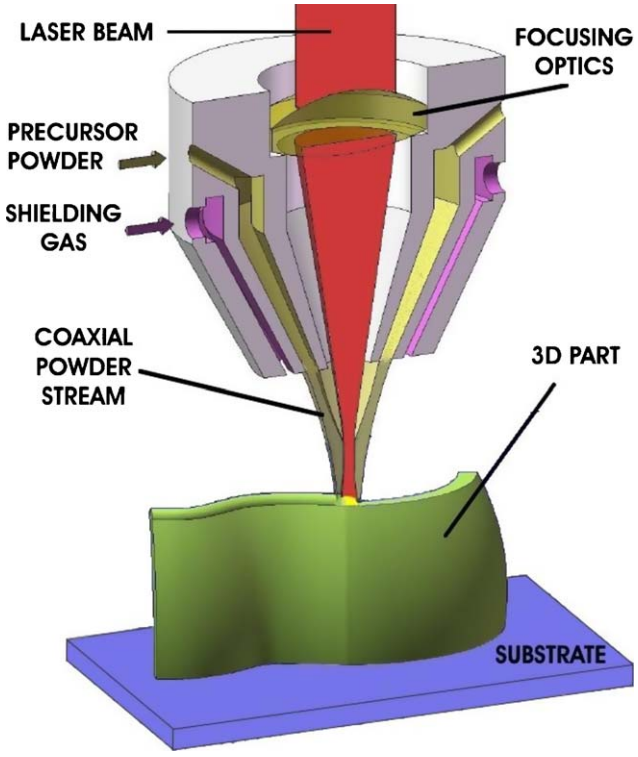

Fig. 1. Sketch showing the principle of operation of rapid prototyping based on laser cladding.

2.2. Rapid prototyping based on laser cladding

The powder feeding technique was applied to obtain the parts by laser surface cladding.[19] This technique consists basically in blowing particles of the precursor material by a carrier gas over the substrate that is moving across this powder flow and the laser beam (see Fig. 1). A stationary high power laser radiation is directed to the surface of the substrate. The laser beam heats up the precursor material cloud and creates a molten pool on the substrate where the particles impinge. To produce a controlled atmosphere around the interaction zone, a shielding inert gas is applied. Solidification takes place when the molten pool goes away from the laser irradiated area; thus, a solidified material strip is formed over de initial substrate. A layered part is built when superposing several strips.

The laser source was a Nd:YAG laser ($\lambda = 1064$ nm) with a maximum power of 4000 W (TRUMPF HL 4006D). The laser radiation was guided by means of a 600 μm core diameter fibre and coupled to the working station via expanding and collimating optics; following, the laser beam was focused over the substrate surface, giving a beam spot with diameter of 2 mm at the substrate upper surface. The focusing optics was a cemented doublet of 250 mm focal length.

The hydroxyapatite precursor powder was fed by a Plasma-Technik powder feeder (model Twin-system 10-C) and injected in the interaction zone by means of a coaxial gas-solid injector. Argon was used as both conveying gas and protective gas, with a

conveying gas volumetric flow of 8.0 l/min and a protective inert gas volumetric flow of 16 l/min. During the experimentation the working head, including the focusing optics and the powder injection system, was moved in the vertical direction (z-axis), whereas the substrate was moved in a horizontal plane (x- and y-axis), the three axes where integrated in a computer numerical control station.

The optical power of the laser beam was varied from 80 to 200 W, with precursor powder mass flow values comprised between 3.7 and 20.4 mg/s, and substrate scanning speeds between 0.8 and 6.7 mm/s. During processing, a coaxial camera was used to monitor the stability and evolution of the melting pool along the deposited layers. The average temperature of the laser–material interaction area was remotely measured by means of a pyrometer, the obtained data should be considered only qualitatively due to variability of the material emissivity during processing.

2.3. Physical and chemical characterization

The obtained samples were geometrically characterized by means of a stereoscopic microscope equipped with an XY positioning stage (Nikon SMZ-10A). To determine the geometry dependence on processing parameters, the layer thickness and width were measured in samples obtained with different conditions. The thickness of the deposited layers determines the geometrical resolution in the vertical direction and the surface roughness of the processed sample, while the layer width determines the geometrical resolution in the horizontal plane. The samples microstructure and elemental composition were examined via scanning electron microscopy (SEM Philips XL-30) and an energy dispersive X-ray spectroscope coupled to the microscope (EDS EDAX PV9760). To obtain quantitative Ca/P values for the analysed calcium phosphate phases, three calcium phosphate standards certified by atomic absorption spectroscopy and X-ray fluorescence were used (Ca/P certified values: 1.00 ± 0.01; 1.70 ± 0.02 and 2.00 ± 0.01). EDS spectra were obtained with beam energy 15 keV, acquisition time 50 s and magnification 1500×; and Ca and P X-ray lines intensity ratios were determined for each calcium phosphate phase. The calibrated Ca/P ratio values were obtained taking into consideration the measured Ca and P X-ray lines intensity ratios of the standards.

Chemical composition and crystallinity was determined by means of X-ray fluorescence spectroscopy (XRF, Siemens SRS 3000) and X-ray diffraction (XRD, Siemens D-5000), respectively. In order to obtain an estimation of the phase weight distribution in the laser processed samples, bi-component mixtures of HA-TTCP and α-TCP-TTCP (HA CAPTAL 90 from Plasma-Biotal UK; α-TCP and TTCP from Clarkson Inc.) were analysed by XRD to obtain the calibration curve weight-peak integrated intensity ratio according to the method proposed in.[27] Due to the elevated content of α-TCP and TTCP crystalline phases, the peak integrated intensity of TTCP was used as reference instead of that of HA. Similarly, mixtures with known proportion of HA and amorphous calcium phosphate (ACP CAPTAL Plasma-Biotal UK) were explored by XRD. In the 2θ range between 15° and 40° the areas below the diffractogram corresponding to crystalline material and amorphous material were measured in order to estimate the amorphous phase content of the laser processed samples.[28]

Fourier transform infrared (FT-IR) spectra of the overall samples were acquired between 400 and 4000 cm^{-1} with a Thermo Nicolet 6700 spectrometer. The typical acquisition conditions were 4 cm^{-1} of resolution, averaging of 32 scans, an apodization Happ-Genzel, a Mertz phase correction, and zero filling 2. To examine structural differences within the sample a Continuum IR microscope coupled to the spectrometer was used to collect the reflectance FT-IR spectra between 650 and 4000 cm^{-1}, scanning $100 \times 100\ \mu m^2$ areas along the sample surface and cross-section.

Raman reflection spectra were recorded by means of a Horiba Jobin Yvon LAbRam-HR800 spectrometer provided with an Ar laser excitation source (488 nm) and also coupled with a microscope. Raman reflection spectra were acquired between 200 and 4000 cm^{-1}. Raman spectra acquisition settings were 40 s/scan, 15 average scans per measured range, and 2 μm of spot size.

2.4. Biological response characterization

2.4.1. Cell culture

The biological performance of the material was assessed by using the pre-osteoblastic cell line MC3T3-E1. This cell line has been established from C57BL/6 mouse calvaria, and it was obtained from the European Collection of Cell Cultures (ECACC, UK). The cells were cultured in MEM-alpha (Sigma, USA) supplemented with 10% Foetal Bovine Serum (FBS; Invitrogen, USA) and were maintained at 37 °C in a humidified atmosphere with 5% of CO_2.

Laser cladding processed samples of $10 \times 10\ mm^2$ in area were cleaned by applying several cycles of 15 min in an ultrasound waterbath with milli-Q water, absolute ethanol and acetone, followed by air drying inside a laminar flow chamber. Following, samples were autoclaved for 15 min at 121 °C. Four samples were inspected by SEM after the cleaning and sterilization procedure to ensure that the samples kept unaltered previous to cell seeding; no modifications of the samples surface were observed.

2.4.2. Cytotoxicity. Solvent extraction test

The evaluation of cytotoxicity of the material in a non-direct contact cells-material was carried out by means of the solvent extraction test, according the standards EN ISO 10993-5 and 10993-12. This test consists on a cell seeding over the solvent extracts obtained previously from the material. The solvent extraction was carried out by placing the sterilized processed samples on a rotating mixer for 24 h in MEM-alpha supplemented with FBS at 37 °C with a surface area: volume ratio of 2 cm^2/ml. The extracts were diluted with MEM-alpha to obtain 100, 50, 30, 10, 5 and 0% of the original concentration. The same procedure was followed with phenol solution at a concentration of 6.4 g/l in MEM-alpha as positive control and pure MEM-alpha as negative control.

MC3T3-E1 cells were cultured in 96-well tissue culture plates at a concentration of 1.7×10^5 cells/ml. Cells were grown to confluent layers in a volume of 100 μl. The different dilutions of the extracts were incubated with the cells for 24 h. Three wells per material and extract concentration were used.

The cellular activity was quantified with the Cell Proliferation Kit I (MTT) from Roche Molecular Biochemicals. This colorimetric assay is based on the reduction of the yellow tetrazolium salt MTT (3-(4,5-dimethyltyazolyl-2)-2,5-diphenyl tetrazolium bromide) into insoluble purple formazan crystals by the mitochondrial enzyme succinate dehydrogenase, only present in living cells.

After the incubation period, 10 μl of the MTT labelling reagent in PBS were added to each well at a final concentration of 0.5 mg/ml. Cells were incubated for 4 h under culture conditions (37 °C, 5% CO_2 and humidified atmosphere) to allow the production of purple formazan crystals. In order to dissolve these formazan crystals, 100 μl of a solution containing 10% SDS in 0.01 M HCl was added to each well. The plate was incubated overnight and the resulting coloured solution was quantified at 570 nm using a Bio-Rad Model 550 microplate spectrophotometer. Data are presented as mean ± standard deviation ($n = 3$). Error bars in figures represent standard deviations.

2.4.3. Cell adhesion and morphology. SEM

Cell adhesion and morphology was assessed in a direct contact cells-material assay. Sterilized samples were placed in 24-well tissue cultured plates**.** MC3T3-E1 suspension of 2.5×10^4 cell/ml in 1 ml of MEM-alpha (Sigma, USA) supplemented with 10% Foetal Bovine Serum (FBS; Invitrogen, USA) was added to each well and the culture medium was renewed every 2–3 days. Cell seeding was carried out directly over the modified surface which was the section analysed.

After each incubation time (1, 3 and 7 days), the three replicates of each experiment were fixed with 2% glutaraldehyde in 0.1 M pH 7.4 cacodylate buffer for 2 h at 4 °C. Samples were then washed three times for 30 min each with cacodylate buffer 0.1 M and dehydrated in graded ethanol solutions (30%, 50%, 70%, 80%, 95%) for 30 min each solution and in absolute ethanol for 1 h. After the dehydration, samples were submitted to an increasing amylacetate:ethanol mixture (25:75, 50:50, 75:25, 15 min each) and to pure amylacetate twice for 15 min. The critical point of CO_2, at 75 atm and 31.3 °C was the final step. The samples were finally mounted on metal stubs and sputter-coated with gold prior to their analysis using a Philips XL 30 Scanning Electron Microscope.

3. Results

3.1. Processing parameters

The working window to produce walls by piling up layers was explored during experimentation. Laser power, precursor powder mass flow and scanning speed were the parameters under study. The objective was to produce a smooth and continuous part growth when processing, and to achieve a homogeneous solid sound part.

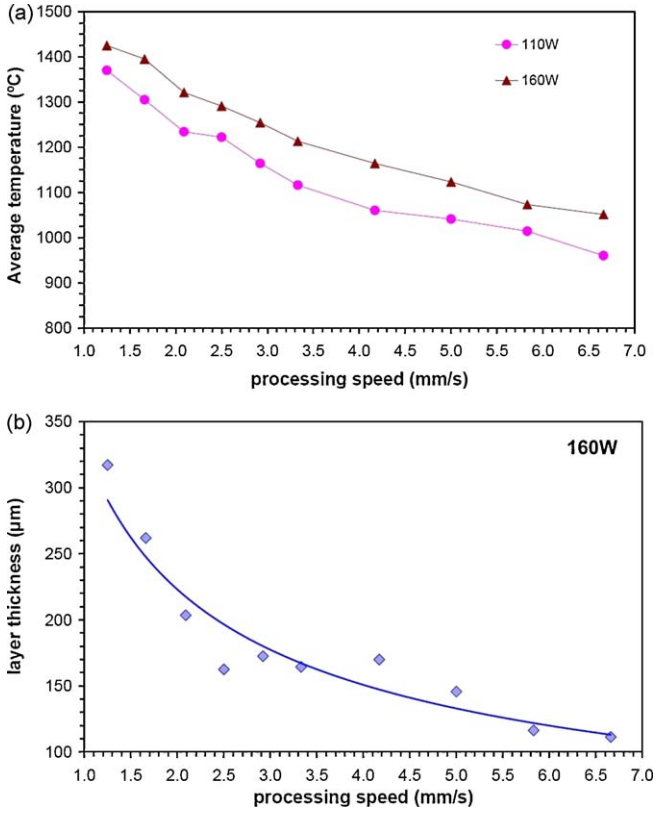

Fig. 2. Evolution of (a) molten pool measured temperature and (b) layer thickness as a function of the processing speed (processing conditions: mass flow 6.7 mg/s, Ar protective gas stream).

The data acquired by means of the camera set coaxial to the laser beam clearly show the presence of liquid material forming the melting pool. In addition, the produced layer thicknesses are comparable to the precursor particles size, indicating that particle geometry was not maintained and that the precursor material was subjected to more transformations than merely sintering. When increasing the processing speed, a reduction of the interaction area temperature is observed (see Fig. 2), attributed to the reduction of absorbed laser energy per part length unit. Consequently, the deposited layer thickness and the obtained part width are reduced by increasing the processing speed.

Fig. 3 shows the influence of the precursor material mass flow on the interaction area temperature and the layer average thickness. At low material injection rates the measured temperature remains invariable. Nevertheless, at high mass flow values important temperature reduction is produced due to an excess of injected precursor material in the interaction area. As a consequence, the thickness of the deposited layers is increased by increasing mass flow rates, but reaches a maximum and stabilizes at high mass flow rates. The produced part width is not significantly modified by the precursor material mass flow variations within the explored range.

The cooling-off part of the thermal cycle experimented by the processed part at the surface was measured and cooling-off speed was estimated for different settings of processing parameters. When cooling rates achieved values as high as 1000 °C/min, the processed part was not able to withstand the high thermal stresses

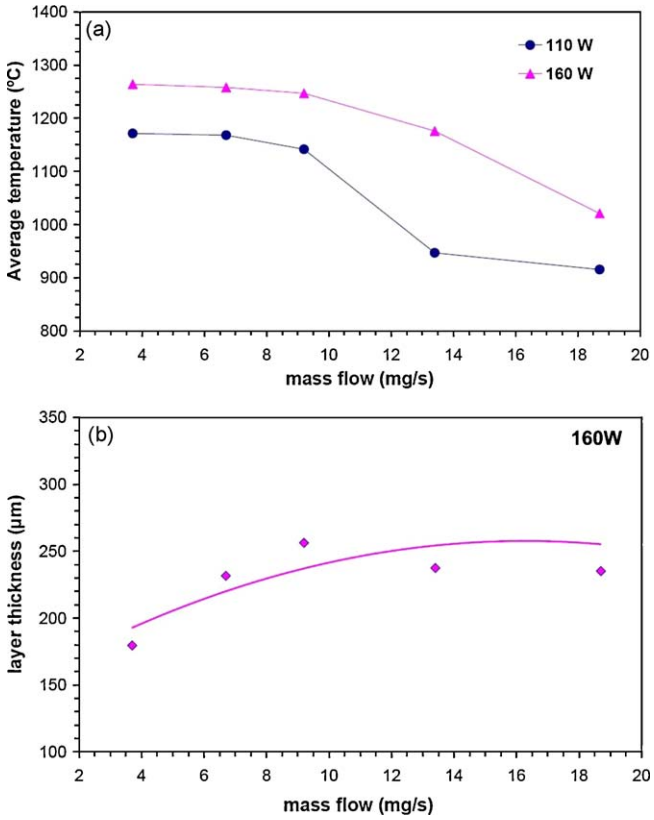

Fig. 3. Evolution of (a) processed part molten pool measured temperature and (b) layer thickness as a function of the precursor powder mass flow (processing conditions: processing speed 2.5 mm/s, Ar protective gas stream).

generated resulting in catastrophic cracking of the part. On the contrary, reducing the cooling speed value to approximately 100 °C/min allows obtaining parts free of cracking. Samples with height up to 60 mm were produced maintaining this cooling rate (see Fig. 4). In addition, the soundness of the processed parts seems to be mainly independent of the cooling-off speed below approximately 1000 °C. Therefore, after depositing the last layer of the processed part further laser irradiation at low power is required to ensure a relatively slow cooling-off at the last layers. Fig. 5 shows the thermal evolution of the upper layers of a processed part, the temperature was measured at the lateral surface and the abrupt turn at 225 s corresponds to the moment when the laser beam is switched off.

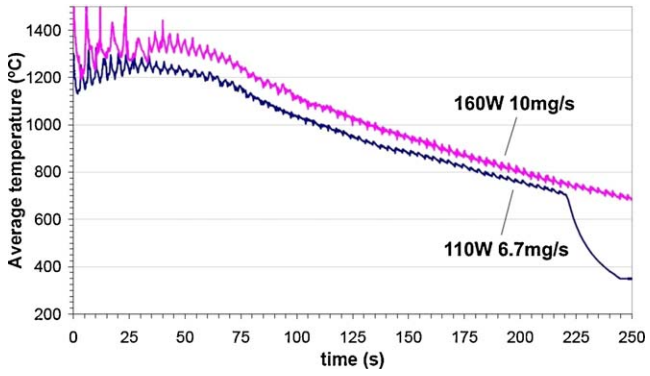

Fig. 5. Thermal evolution of the upper layers of processed parts in two different conditions, the temperature was measured at the lateral surface. The abrupt turn at 225 s in the curve at 110 W corresponds to the moment when the laser beam is switched off (processing conditions: processing speed 2.92 mm/s, Ar protective gas stream).

3.2. Composition and microstructure

3.2.1. FT-IR spectra and XRD analysis of the complete processed sample

The FT-IR spectrum of the HA precursor powder and that corresponding to a complete processed sample transformed

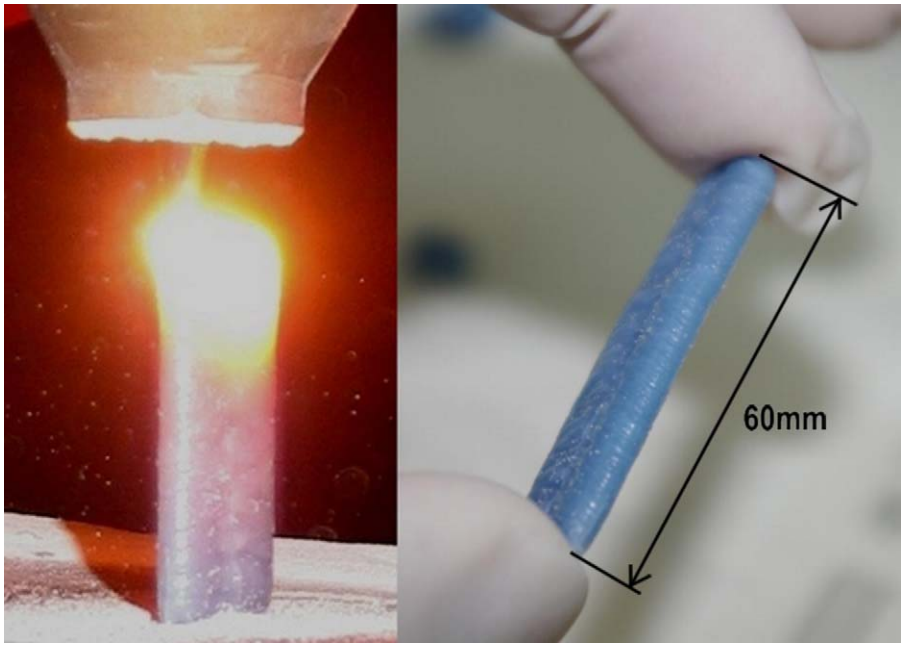

Fig. 4. Calcium phosphate sample produced by rapid prototyping based on laser cladding (complete sample height 60 mm, laser power 160 W, scanning speed 3.0 mm/s, mass flow 10 mg/s, 320 stacked layers).

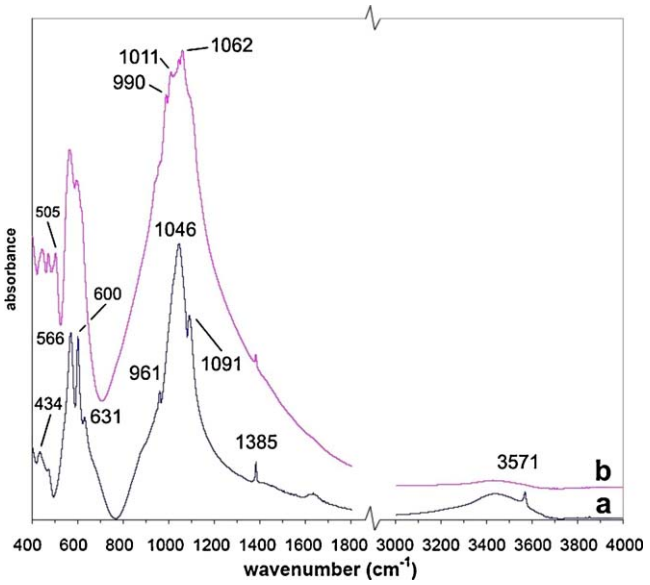

Fig. 6. FT-IR reflection spectra of (a) HA precursor material and (b) sample processed by laser cladding after pulverization.

into powder are shown in Fig. 6. The bands corresponding to the phosphate group are clearly distinguished in both spectra. The antisymmetric stretching vibrational modes (ν_3 PO_4^{3-}) are found between 990 and 1100 cm^{-1}. In the precursor HA spectrum, the symmetric stretching mode (ν_1 PO_4^{3-}) is present as a small peak at 961 cm^{-1}, whereas only a shoulder is observed in the processed samples spectra due to the splitting of ν_3 peaks and band broadening. The peaks corresponding to symmetric bending (ν_2 PO_4^{3-}) are found between 400 and 500 cm^{-1}; and peak splitting is also observed in the processed samples spectra. The peaks related to out-of-plane modes (ν_4 PO_4^{3-}), located between 550 and 600 cm^{-1}, show slightly displacements to lower wavenumbers.

The low presence of CO_3^{2-} could be suggested from the weak shoulder around 875 cm^{-1} observed in the HA precursor powder spectra, while no indication of CO_3^{2-} groups presence was found in the processed samples spectra.

The presence of OH^- groups in the HA precursor material is observed by the peaks at 631 and 3571 cm^{-1}. These peaks were not observed in the laser processed material spectrum; indicating that complete HA dehydroxylation has been produced during laser processing. The absorbed water is presented by a broad band around to 3400 cm^{-1} and a weaker band at 1635 cm^{-1} in both spectra.

The XRD analyses of the material processed by laser cladding were performed after pulverization of the complete samples (see Fig. 7). The diffraction patterns match with the XRD patterns of HA (JCPDS 9-432), α-TCP (JCPDS 9-348) and TTCP (JCPDS 25-1137) crystals. The more intense peaks correspond to α-TCP and TTCP, whereas the HA attributed overlapped peaks could produce the observed peak broadening. In addition, previously to baseline correction, a broad band was observed in the diffractogram, indicating that amorphous phases are present in the processed samples. The areas corresponding to crystalline material and amorphous material (ACP) below the processed

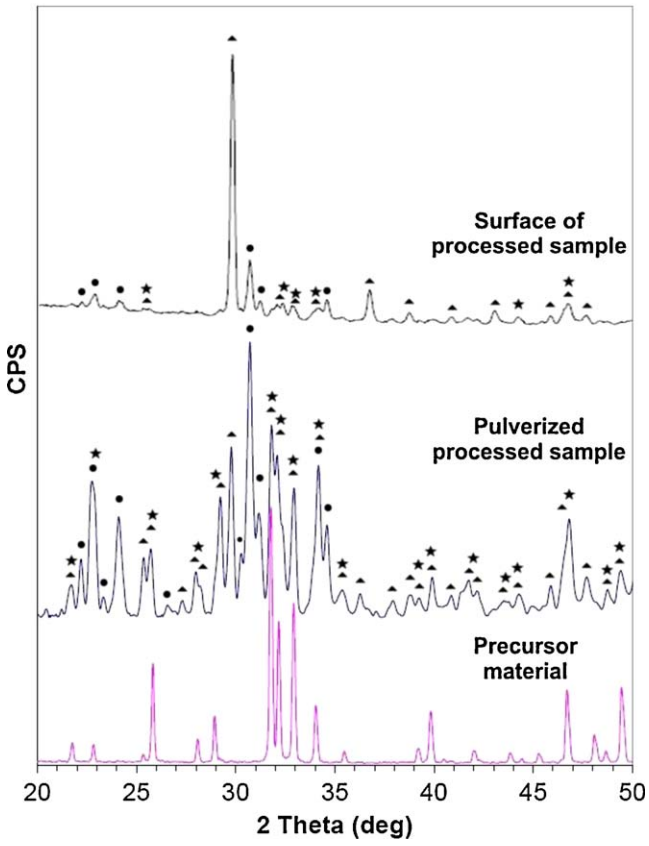

Fig. 7. X-ray diffractogram of: hydroxyapatite precursor powder; pulverized processed sample; surface of the processed. (▲) TTCP (JCPDS 25-1137), (●) α-TCP (JCPDS 9-348), (⋆) HA (JCPDS 9-432). The broad band between 15° and 35° indicating presence of amorphous phase was eliminated by baseline correction.

samples diffractograms were measured, and the estimation from the calibration curve revealed an average amorphous phase weight content value of 40%. The proportions of crystalline and amorphous phases estimated from the XRD data are summarized in Table 2. No peaks related to crystalline CaO and $CaCO_3$ presence are observed in the samples XRD pattern; and no determining information is obtained about the presence of $Ca(OH)_2$ due to peak overlapping with TTCP and α-TCP peaks.

Although most of the HA XRD peaks overlap with TTCP peaks, presence of HA or oxyapatite (OA) is derived from the peak at $2\theta = 10.8°$ (see Fig. 8). HA and oxyapatite, produced by dehydroxylation of HA, present a very similar XRD pattern; nevertheless, due to oxyapatite larger c-axis, the HA peak at $2\theta = 53.1°$ is shifted to smaller angles in oxyapatite

Table 2
Crystalline and amorphous phase content estimated from the XRD data (% weight).

Calcium phosphate phase	Content (% weight)
ACP	40 ± 4.2
α-TCP	29 ± 3.8
TTCP	18 ± 2.7
OA	13 ± 2.3

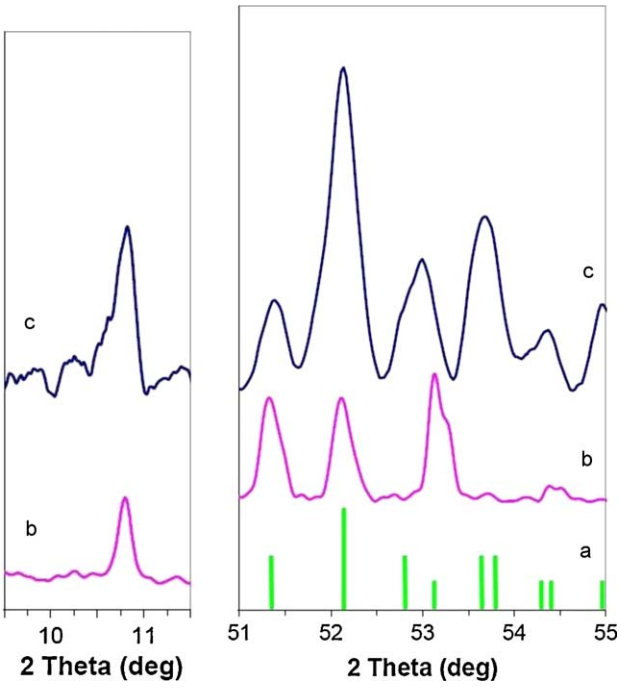

Fig. 8. X-ray pattern of (a) TTCP (JCPDS 25-1137) and diffractograms of (b) hydroxyapatite precursor powder and (c) pulverized processed sample. Details of the peaks at $2\theta = 10.8^\circ$ and $2\theta = 53.1^\circ$, both graphs have the same *y*-axis intensity scale.

diffractogram.[29] Detail of the laser processed samples diffractogram around $2\theta = 53.1^\circ$ is compatible with the mentioned peak shift as shown in Fig. 8; but no determinant conclusions can be extracted due to presence of TTCP peaks in this diffractogram zone.

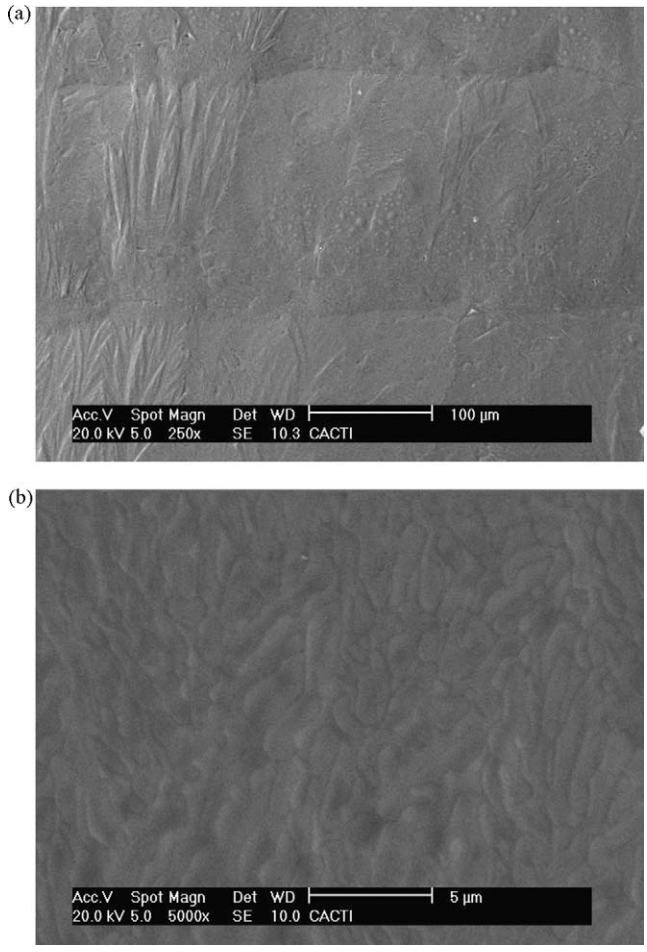

Fig. 9. SEM micrographs of the sample surface (a) at low magnification and (b) detail of the oriented surface grains.

3.2.2. *Surface characterization*

Sample surfaces topography are smooth, as revealed by SEM secondary electrons micrographs, and the appearance suggests complete melting of the deposited material at the surface, without sintered or semimolten HA particles. Fig. 9a shows the lateral surface of one deposited layer, with an average thickness of 170 μm. Observation at higher magnification allows to distinguish a main structure of elongated grains with rounded corners,

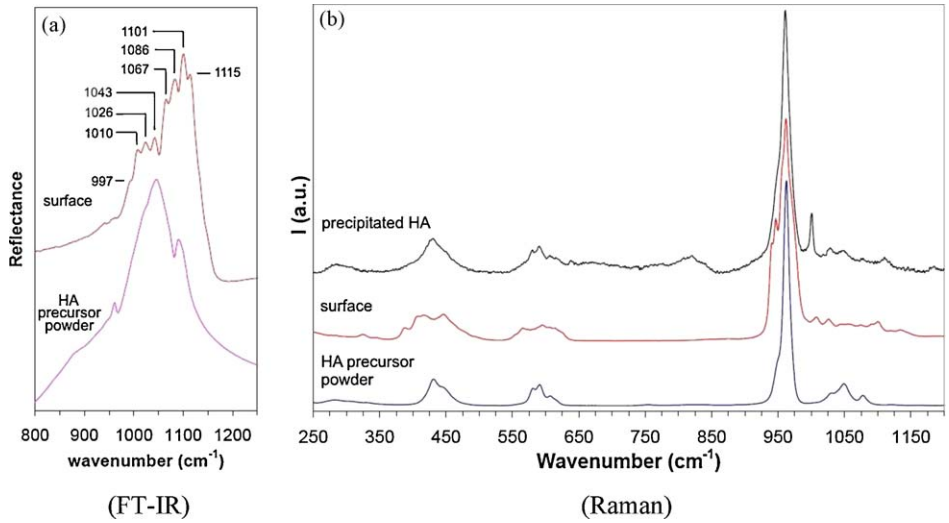

Fig. 10. (a) FT-IR reflection spectra of the sample surface and the HA precursor powder; (b) representative Raman spectra of the surface, the HA precursor powder and the precipitated HA after 7 days in cell culture.

with an average length of $2.5 \pm 0.60\,\mu m$ and average width of $0.65 \pm 0.14\,\mu m$ (Fig. 9b). The grain predominant direction is transversal to the direction of layer stacking.

A typical FT-IR spectrum acquired at the processed samples surface is shown in Fig. 10a. In the surface spectra, the band corresponding to the P–O symmetric stretching vibration mode (ν_1 PO_4^{3-}) appears very weakly as a shoulder in 960 cm^{-1} and the triply degenerate antisymmetric stretching modes of the PO_4^{3-} group (ν_3 PO_4^{3-}) rise strongly between 990 and 1115 cm^{-1}. Splitting of ν_3 PO_4^{3-} peaks is produced for the processed samples. Due to the specific configuration of the spectrometer when using the coupled microscope, the wavenumbers below 650 cm^{-1} were not acquired.

Raman spectra clearly show the presence of phosphate groups in the samples surface (see Fig. 10b). The stronger observed peak at 962 cm^{-1} corresponds to the ν_1 PO_4^{3-} mode. Two more peaks of lower intensity are found at 947 and 942 cm^{-1}, indicating the presence of TTCP. The ν_3 PO_4^{3-} antisymmetric stretching modes rise timidly between 1000 and 1150 cm^{-1}, in contrast to the related peaks in the FT-IR spectrum. Although the band at 1101 cm^{-1} could be also assigned to ν_1 CO_3^{2-} vibration mode; nevertheless, this attribution is discarded as no peaks corresponding to ν_4 CO_3^{2-} mode are observed around 675 cm^{-1} and 765 cm^{-1}.[30]

Splitting of peaks corresponding to ν_2 PO_4^{3-} vibration modes is found between 389 and 447 cm^{-1}; and also of the ones related to ν_4 PO_4^{3-} modes appear between 556 and 614 cm^{-1}. No indication of OH^- group presence was observed around 3570 cm^{-1} (spectrum zone not shown). In a similar manner, the 3618 cm^{-1} peak of OH^- stretching in $Ca(OH)_2$ is not observed in the Raman spectra, indicating $Ca(OH)_2$ absence in the processed samples.

Raman and FT-IR spectra of the samples surface are in agreement with the reported polycrystalline TTCP Raman and FT-IR spectra, respectively.[31]

The XRD analyses of the samples surfaces match with the α-TCP, TTCP, and HA XRD patterns. The diffractograms are dominated by a strong TTCP peak (0 4 0), indicating that the TTCP crystals are preferentially oriented, Fig. 7. This preferential growth of TTCP crystals from laser processed HA, already observed in previous studies, is attributed to well-defined thermal gradient at the sample surface when the material is cooling off.[32] During processing, the material convection due to high thermal gradient is parallel to the sample surface, in the direction coincident to the sample growth and perpendicular to the deposited layer plane, leading to a very stable solidification front direction that produces the observed grain alignment.

3.2.3. Cross-section characterization

SEM examination of samples cross-section reveals the presence of different phases as shown in Fig. 11. The backscattered electron micrographs allow distinguishing brighter grains with irregular shapes dispersed over the entire cross-section. The morphology of these grains suggests that incomplete melting of the material has taken place. In coexistence and dispersed within a darker phase, elongated grains with rounded corners similar to those observed at the samples surface are found. In the sample

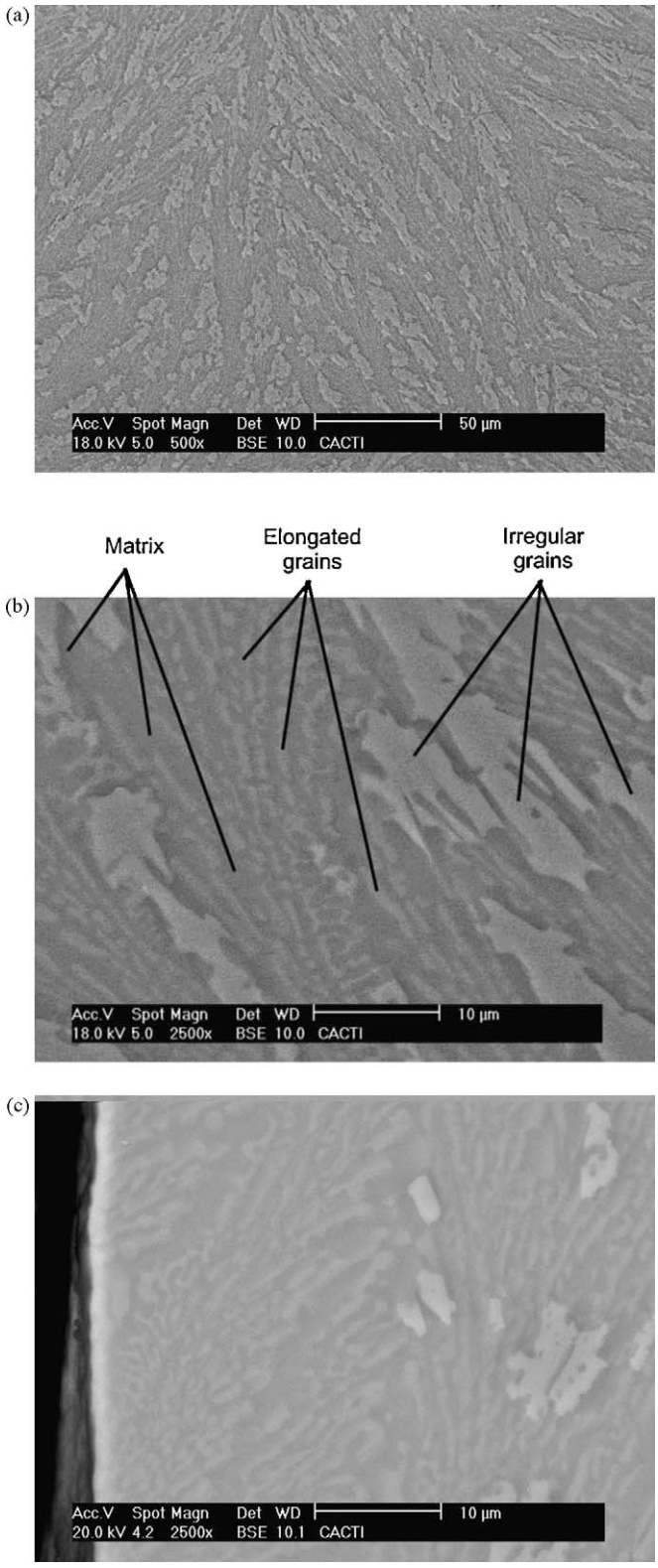

Fig. 11. SEM micrographs of the sample cross-section: (a) sample central zone, (b) detail of the microstructure at the central zone, and (c) detail of the microstructure close to sample surface.

Table 3
Ca/P ratio values (molar) of the HA precursor powder, the sample phases and the precipitated HA after cell culture (from the EDS microanalysis).

	Ca/P (molar)
HA precursor material	1.72 ± 0.08
Matrix	1.53 ± 0.03
Elongated grains	1.87 ± 0.06
Irregular grains	1.62 ± 0.06
Precipitated HA in cell culture	1.60 ± 0.05

central zone, Fig. 11a and b, and in the zone close to the surface (Fig. 11c), the grains are strongly oriented. Although sample charging at the edge makes difficult the examination, as shown in Fig. 11c, the elongated grains seems to converge at the cross-section edge, which is in agreement with the observations made at the surface of the samples. From the samples surface towards the centre no unmolten irregular brighter grains are found within a band of 20 μm depth.

The EDS microanalyses of each observed phase were performed at different zones of the samples cross-section, and reveal the Ca/P values listed in Table 3. Standards with certified Ca/P ratios were used to obtain these quantitative values, which suggest that the microstructure corresponds to a TTCP dispersed grains in a α-TCP matrix, with the presence of remainder apatite irregular grains (Fig. 11b). The XRD patterns obtained from the samples cross-section are equivalent to those acquired from the complete pulverized samples, from these can be derived that amorphous material is present in the cross-section. Since irregular grains are present in the samples cross-section and not in the surface, and amorphous material is not observed from the surface XRD pattern, it can be concluded that the irregular grains are related to amorphous calcium phosphate. Both the cross-section and the surface microstructure were confirmed to keep invariable along the processed sample height by SEM observation and XRD analyses.

With the aim of improving phase identification, Raman spectra were acquired from each phase in different zones at the cross-section, and the averaged spectra were compared with the precursor HA, commercial TTCP and α-TCP materials Raman spectra (see Fig. 12). The elongated grains averaged spectrum (Fig. 12, spectrum f) closely mach the spectrum of TTCP, being in agreement to the measured Ca/P ratio value. The ν_1 PO_4^{3-} strong peaks at 942, 947, 957 and 963 cm^{-1} and the lattice modes at 329 and 350 cm^{-1} allow to clearly distinguish this calcium phosphate compound. In the ν_2 PO_4^{3-} zone of the averaged spectrum of the matrix phase (Fig. 12, spectrum e), the band around 420 cm^{-1} and the peak at 450 cm^{-1} match the α-TCP spectrum, although low presence of TTCP can be derived from the weak peaks at 329, 350 and 391 cm^{-1}. In the ν_1 PO_4^{3-} region, presence of TTCP peaks are observed in addition to the strong peak at 963 cm^{-1}, common to α-TCP, TTCP and HA compounds. At higher wavenumbers of this peak is observed a pronounced shoulder attributed to the α-TCP peak at 972 cm^{-1}. Regarding the irregular grains, the averaged spectrum is different from the other spectra in the band around 306 cm^{-1} and a strong ν_2 PO_4^{3-} at 440 cm^{-1}. In addition, the ν_1 PO_4^{3-} zone a broad peak at 964 cm^{-1} is accompanied by a shoulder at 950 cm^{-1}, attributed to amorphous calcium phosphate.

3.3. Biological response characterization

3.3.1. Cytotoxicity. Solvent extraction test

Results regarding cytotoxicity (MTT Assay) of HA laser cladding processed samples are shown in Fig. 13. MC3T3 cells proliferated properly on the different dilutions of the solvent extracted from the tested material. A slight deviation from the negative control (pure culture medium MEM-alpha) is observed when adding extracts from processed samples; nevertheless, variance analysis states that differences between processed samples and negative control at each concentration are not statistically significant ($p < 0.05$). This healthy stage of cells indicated that laser cladding processed HA samples were non-cytotoxic. At the same time, the cytotoxicity shown by the positive control validated the experiment.

3.3.2. Cell adhesion and morphology. SEM

To evaluate the cell attachment, spreading, and proliferation, three replicates from laser cladding processed samples were analysed at 1, 3 and 7 days by scanning electron microscopy. SEM micrographs of the MC3T3-E1 pre-osteoblasts on the surface of the laser cladding processed samples throughout the time of culture (A for 1 day, B for 3 days and C for 7 days) are

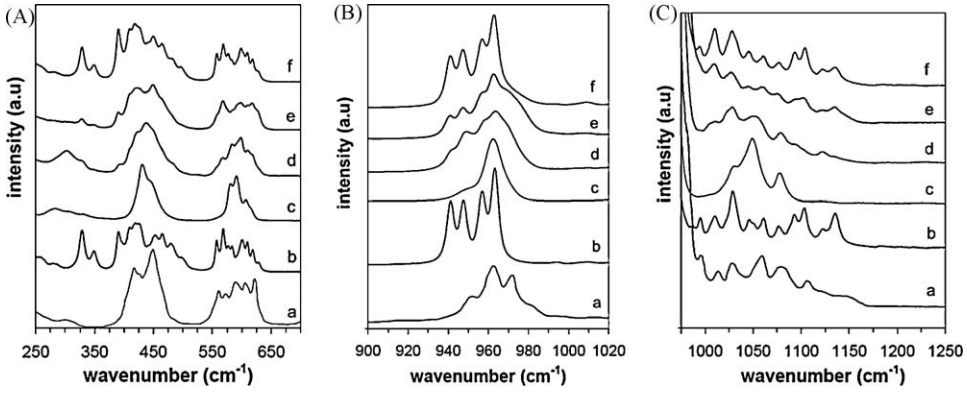

Fig. 12. Raman spectra in the (A) ν_2 and ν_4 region, (B) ν_2 region and (C) ν_3 phosphate region. Shown spectra were acquired from (a) commercial α-TCP, (b) commercial TTCP, (c) HA precursor powder and from the laser processed samples cross-section: (d) irregular grains, (e) matrix, (f) elongated grains.

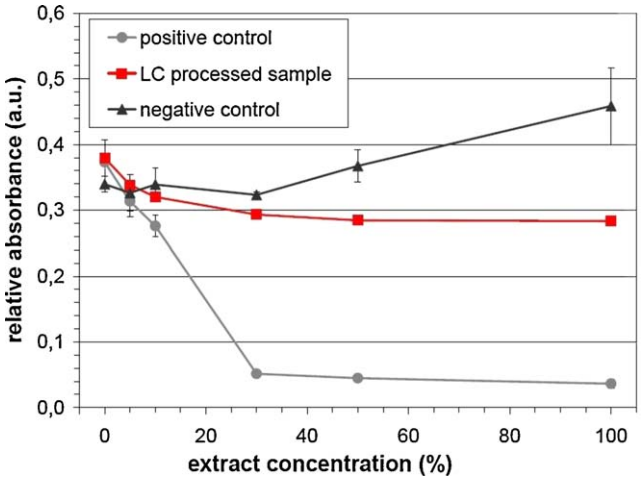

Fig. 13. MC3T3-E1 proliferation after incubation with different dilutions of the solvent extracts prepared from the laser cladding processed HA surface. The negative control consisted of pure MEM-alpha and the positive control was composed by a phenol solution at a concentration of 6.4 g/l in MEM-alpha.

presented in Fig. 14. On the first day of incubation (A), it was already observed a precipitation process of apatite that occurred parallel to the cell proliferation due to the presence of the high soluble α-TCP and TTCP phases immersed in MEM-alpha supplemented with 10% Foetal Bovine Serum. Some of those apatite crystals are shown in Fig. 15. The Raman spectrum of the precipitated apatite is shown in Fig. 10b. In addition to characteristic peaks of HA, broad bands around 675 and 820 cm^{-1} are observed due to organic material presence; the sharp peak at 1002 cm^{-1} can be attributed to HPO_4^{2-} ν_1 mode and phenylalanine presence from the cell culture media. It was confirmed by EDS microanalysis that the precipitated apatite was calcium-deficient hydroxyapatite (see Table 3). Regarding to the cellular behaviour, cells appeared closely attached to the processed samples surface and also to the precipitated apatite with the flattened morphology typical of healthy osteoblasts and numerous filopodia. After 3 days of incubation (B), the cells connect to each other by filopodia and lamellipodia and spread throughout the surface, even over or below the precipitates. When observed on the seventh day of incubation (C), several layers of cells covered almost the whole surface, including the numerous CDHA precipitates. Cells attach and spread properly, without any signal of cytotoxicity.

4. Discussion

According to the $CaO–P_2O_5$ phase diagram and HA decomposition experimental studies, dehydroxylation of HA into oxyhydroxyapatite starts at 900 °C and is produced gradually depending on the exposition time at these high temperatures.[33,34] Oxyhydroxyapatite (OHA, $Ca_{10}(PO_4)_6(OH)_{2-x}O_x$) subjected to a further thermal treatment starts to decompose into α-TCP and TTCP above 1200 °C, and is fully decomposed at approximately 1550 °C; these temperature values and the calcium phosphate phases obtained are dependent on the processing atmosphere water vapour content. Hydroxyapatite dehydroxylation is not produced completely before decomposition in α-TCP and TTCP and, therefore, the presence of these last mentioned calcium phosphate phases is compatible with OHA presence.[35] Due to their crystal structure resemblance, XRD patterns of oxyapatite (OA, $Ca_{10}(PO_4)_6O_2$, obtained after complete HA dehydroxylation), oxyhydroxyapatite and hydroxyapatite are very similar; therefore, is difficult to establish the grade of dehydroxylation from the acquired XRD patterns. The complete absence of the OH^- group peaks in the FT-IR spectra of processed samples suggests that all the present apatite corresponds to oxyapatite. Taking this fact into consideration, the XRD peaks attributed to crystalline HA phase correspond actually to crystalline oxyapatite. Oxyapatite is reported to be stable only between 800 and 1050 °C, but HA subjected to 1250 °C for 1 h after being melted showed a FT-IR spectrum without

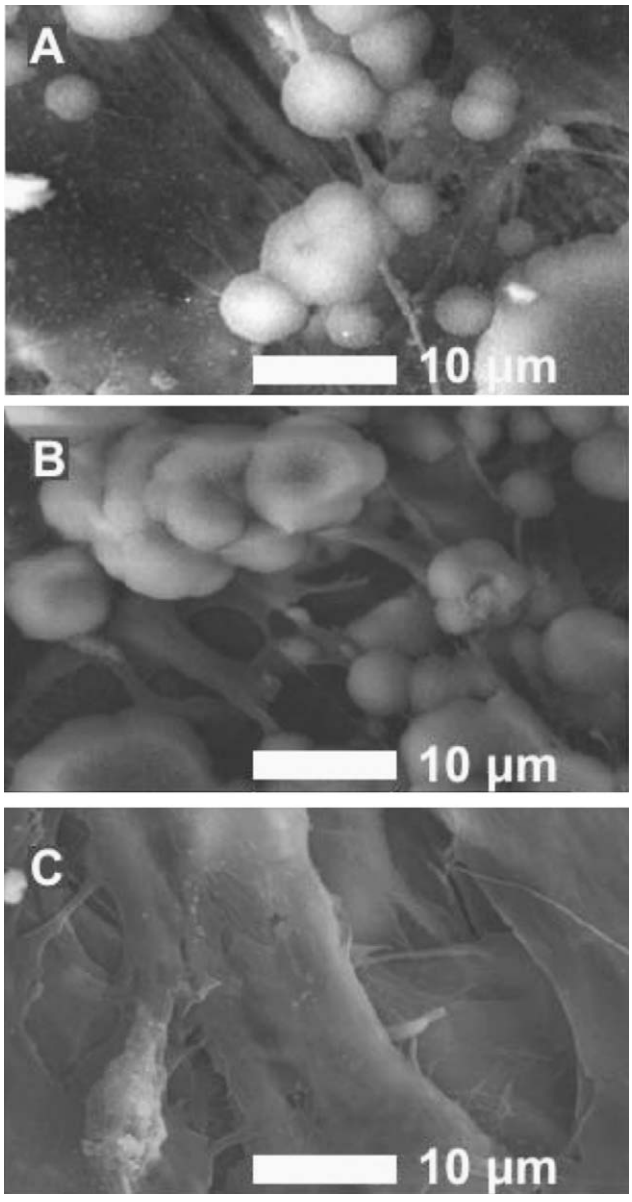

Fig. 14. Scanning electron microscopy images showing the attachment and spreading of MC3T3-E1 cell line on laser cladding processed samples surface. A for 1 day, B for 3 days and C for 7 days. Magnification 2500×.

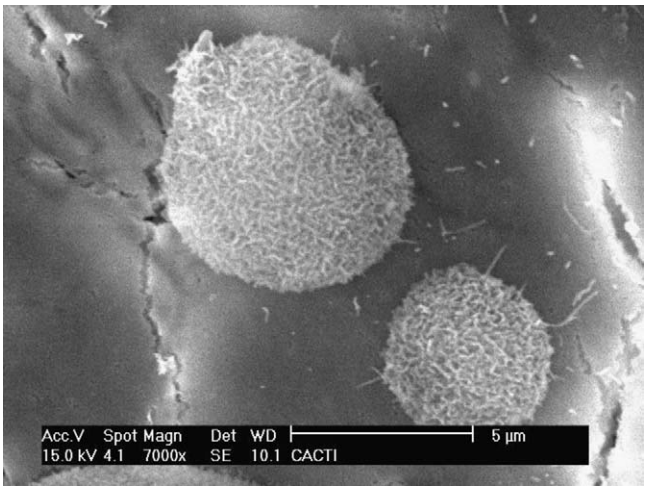

Fig. 15. Scanning electron microscopy image showing the calcium-deficient hydroxyapatite precipitated crystals on to a cell layer covering the laser cladding processed sample.

OH presence and a XRD pattern with clear presence of OA (occasionally identified as HA).[35,36]

During laser cladding processing, the injected HA precursor powder irradiated by the laser beam suffers a prominent temperature increment in a reduced period of time, this high heating rate produces that not all HA particles are fully decomposed in α-TCP and TTCP. Therefore, the obtained melting pool is composed by a combination of a liquid phase and a remaining solid phase that could correspond to non-decomposed OA and mixtures of α-TCP and TTCP. Some authors consider that α-TCP and TTCP formation occurs at the same temperature[3]; while others state that HA decomposes in α-TCP and CaO, forming TTCP at higher temperature by combination of α-TCP and CaO,[34] being these differences attributed to different experimental conditions. The microstructure observed in the laser processed samples suggests that the TTCP grains could be formed from the liquid material when cooling off instead from HA decomposition during heating.

When the molten pool starts to cool down, attending to the microstructure observed by SEM, the TTCP nucleates first from the liquid phase and from the boundaries of remainder solid grains, leading to the observed TTCP rich dispersed grains. Simultaneously, the liquid phase increases its PO_4 content and solidifies into the observed α-TCP rich matrix. Diffusion within the solid mixture of calcium phosphates can also modify the phase composition at elevated temperature values.

For the HA precursor material, the heating rate produced by the laser–material interaction is higher than the cooling rate and, moreover, the global material composition changes during processing. Therefore, differences of phase transformations between the heating path and the cooling path are to be expected. The thermal cycle experienced is not exactly identical for all the injected precursor particles, and probably some of them are not exposed to laser radiation time enough to decompose, leading to the found remaining OA grains. In bulk HA subjected to heat treatment, it is observed that decomposition of HA starts from the surface towards the interior.[34] Similarly, in the laser processed samples the observed remaining irregular grains of OA could correspond to the cores of the fed HA precursor particles.

Reconstitution of α-TCP and TTCP into HA is observed to be dependent on the cooling rate and atmosphere.[37] According to the measured cooling rates, recombination of α-TCP and TTCP into HA and transformation from the metastable phase α-TCP to β-TCP is inhibited.

As explained by Ducheyne and co-workers, several steps are involved during bone tissue bonding to bioactive ceramic materials. These steps begin with a dissolution process from ceramic, then precipitation from solution onto ceramic, ion exchange and structural rearrangement at the ceramic-tissue interface, interdiffusion from the surface boundary layer into the ceramic, solution-mediated effects on cellular activity, deposition of either the mineral phase or the organic phase without integration into the ceramic, chemotaxis to the ceramic surface, cell attachment and proliferation, cell differentiation, and extracellular matrix formation.[38] In most cases, the ceramic-tissue interface modifications lead to a calcium-phosphate interface layer. Although the process involves inorganic reactions and biological events interacting together in a not simple sequence, the solubility of the bioactive ceramic plays an important role in several of these reactions composing the overall osteogenesis process. The enhancement effect of bone tissue growth is more boosted for higher solubility rates of the implanted bioactive ceramic.[38–40] α-TCP, and amorphous calcium phosphate (ACP), which are phases present in the laser processed samples, are more soluble in aqueous solutions than other calcium phosphate phases like HA or β-TCP. TTCP present a intermediate solubility between β-TCP and HA.[4,38,41,42]

Pre-osteoblastic cell response to α-TCP and TTCP, respectively, was tested in previous *in vitro* studies.[43] The results showed that presence of α-TCP and TTCP dissolved in the culture medium increases cell alkaline phosphatase activity, and promotes collagen synthesis and calcification of the extracellular matrix. Laser cladding coatings of similar precursor HA material on Ti6Al4V substrates were previously developed, obtaining successful results of *in vitro* tests.[19–21,24] In addition, the α-TCP and TTCP capacity of promoting new bone formation when implanted in bone defects has been reported as a result of *in vivo* studies.[6,44,45] Osteogenesis promotion observed in cell culture of calcium phosphate samples processed by laser cladding is in good agreement with these findings.

Previous *in vitro* studies have evaluated the suitability of α-TCP and ACP combination to be used as calcium phosphate cements in bone restoration applications.[4,46] It was observed that when the combination was immersed in aqueous solution, it reacted to produce calcium-deficient precipitated hydroxyapatite (according to the reaction: $3Ca_3(PO_4)_2{\cdot}nH_2O \Rightarrow Ca_9(PO_4)_5(HPO_4)OH + (3n-1)H_2O$[44]). This calcium-deficient hydroxyapatite obtained as precipitation in the aqueous dissolution of other calcium phosphates, is usually poorly crystalline and can present a Ca/P molar ratio from 1.50 to that of the crystalline stoichiometric hydroxyapatite (Ca/P = 1.67).[43] In the absence of a biologically equivalent, calcium deficient, carbonate containing hydroxyapatite surface

upon implantation, dissolution, precipitation and ion exchange reactions lead to a biologically equivalent apatitic surface on the implanted material.[38] Moreover, according to Kokubo et al.,[47] this calcium-deficient apatite formed on the surface of the laser processed graft is an unambiguous sign of the ability of the material to bond to living bone when inserted into the body.

The physic-chemical and biological studies carried out in this work, allow affirming that the rapid prototyping technique used in this work shows a promising potential to produce useful bioceramic grafts. This technique can be expanded to the production of customized grafts if three-dimensional images of the defect site are used as source for designing the adequate implant and generating the necessary information to drive the laser based rapid prototyping working station. Further work to validate these calcium phosphate grafts obtained by the rapid prototyping based on laser cladding technique is currently under progress, including mechanical testing and "*in vivo*" studies.

5. Conclusions

The application of rapid prototyping based on laser cladding to three-dimensional processing of bioceramic grafts from HA precursor material, reveals that sound structures can be obtained when moderate cooling rates are maintained. Geometrical control of the piled up ceramic layers is possible by means of laser energy density and precursor powder flow modifications.

Processing by laser cladding lead to complete dehydroxylation of the precursor HA, the obtained microstructure is composed by a α-TCP matrix with nucleated TTCP grains, in coexistence with non-decomposed oxyapatite and amorphous calcium phosphate. Due to the produced high thermal gradients, grains of TTCP are preferentially oriented at the samples surface.

The material obtained from HA processing by rapid prototyping based on laser cladding is non-cytotoxic. The produced calcium phosphate grafts lead to calcium-deficient hydroxyapatite precipitation and promote pre-osteoblastic cell attachment and proliferation during "*in vitro*" cell culture test.

Acknowledgments

This work was partially financed by the Spanish Government and FEDER (CICYT MAT2006-10481), FPU program AP2006-03500 grant, and Galician Government (PGIDT06805 AY020031F, INCITE081R303002ES, INCITE09E2R303103ES). Dr. S. Chiussi is gratefully acknowledged for his assistance in Raman spectroscopy. Technical staff of CACTI (University of Vigo) is gratefully acknowledged.

References

1. Younger EM, Chapman MW. Morbidity at bone graft donor sites. *J Orthop Trauma* 1989;**3**:192–5.
2. Schwartz CE, Martha JF, Kowalsi P, Wang DA, Bode R, Li L, et al. Prospective evaluation of chronic pain associated with posterior autologous iliac crest bone graft harvest and its effect on postoperative outcome. *Health Qual Life Outcomes* 2009;**7**:49.
3. Hench LL, Wilson J. *An introduction to bioceramics*. Singapore: World Scientific; 1993.
4. Best SM, Porter AE, Thian ES, Huang J. Bioceramics: past, present and for the future. *J Eur Ceram Soc* 2008;**28**:1319–27.
5. Daculsi G, Laboux O, Malard O, Weiss P. Current state of the art of biphasic calcium phosphate bioceramics. *J Mater Sci Mater Med* 2003;**14**:195–200.
6. Kurashina K, Kurita H, Kotani A, Takeuchi H, Hirano M. In vivo study of a calcium phosphate cement consisting of α-tricalcium phosphate/dicalcium phosphate dibasic/tetracalcium phosphate monoxide. *Biomaterials* 1997;**18**:147–51.
7. Abe K, Ono I. A comparison of the shapes of hydroxyapatite implants before and after implantation. *J Biomed Mater Res Appl Biomater* 2002;**63**:312–8.
8. Quadrani P, Pasini A, Mattioli-Belmonte M, Zannoni C, Tampieri A, Landi E, et al. High-resolution 3D scaffold model for engineering tissue fabrication using a rapid prototyping technique. *Med Biol Eng Comput* 2005;**43**:196–9.
9. Nikopoulos CE, Mavrogenis AF, Petrocheilou G, Kokkinis C, Diamantopoulos P, Papagelopoulos PJ. A three-dimensional medical imaging model for quantitative assessment of proximal tibia vs. anterior iliac crest cancellous bone. *Knee* 2008;**15**:233–7.
10. Griffin A, McMillin S, Griffin C, Barton K. Bioceramic RP materials for medical models. In: *Proceedings of the 7th international conference on rapid prototyping*. 1997. p. 355–9.
11. Webb PA. A review of rapid prototyping (RP) techniques in the medical and biomedical sector. *J Med Eng Technol* 2000;**24**:149–53.
12. Chartoff R, Steidle C, Klosterman D, Graves G, Osborne N. Automated fabrication of custom bone implants using rapid prototyping. Business briefing: medical device manufacturing and technology;2002:10–4.
13. Salgado AJ, Coutinho OP, Reis RL. Bone tissue engineering: state of the art and future trends. *Macromol Biosci* 2004;**2**:743–65.
14. Bertrand Ph, Bayle F, Smurov I. Yttria-zirconia components manufacturing for biomedical applications by SLS technology. In: *Proceedings of the international congress on applications of lasers & electro-optics*. 2007. p. 192–5.
15. Kanczler JM, Mirmalek-Sani SH, Hanley NA, Ivanov AL, Barry JJA, Upton C, et al. Biocompatibility and osteogenic potential of human fetal femur-derived cells on surface selective laser sintered scaffolds. *Acta Biomater* 2009;**5**:2063–71.
16. Wiria FE, Leong KF, Chua CK, Liu Y. Poly-ε-caprolactone/hydroxyapatite for tissue engineering scaffold fabrication via selective laser sintering. *Acta Biomater* 2009;**3**:1–12.
17. Eosoly S, Brabazon D, Lohfeld S, Looney L. Selective laser sintering of hydroxyapatite/poly-ε-caprolactone scaffolds. *Acta Biomater* 2010;**6**(7):2511–7.
18. Xue L, Islam MU. Free-form laser consolidation for producing metallurgically sound and functional components. *J Laser Appl* 2000;**12**:160–5.
19. Lusquiños F, Pou J, Arias JL, Boutinguiza M, Pérez-Amor M, León B, et al. Production of calcium phosphate coatings on Ti6Al4V obtained by Nd:yttrium–aluminum–garnet laser cladding. *J Appl Phys* 2001;**90**:4231–6.
20. Lusquiños F, De Carlos A, Pou J, Arias JL, Boutinguiza M, León B, et al. Calcium phosphate coatings obtained by Nd:YAG laser cladding: physicochemical and biologic properties. *J Biomed Mater Res* 2003;**64A**:630–7.
21. Lusquiños F, Pou J, Boutinguiza M, Quintero F, Soto R, León B, et al. Main characteristics of calcium phosphate coatings obtained by laser cladding. *Appl Surf Sci* 2005;**247**:486–92.
22. Kurella A, Dahotre NB. Laser induced hierarchical calcium phosphate structures. *Acta Biomater* 2006;**2**:677–83.
23. Roy M, Krishna BV, Bandyopadhyay A, Bose S. Laser processing of bioactive tricalcium phosphate coating on titanium for load-bearing implants. *Acta Biomater* 2008;**4**:324–33.
24. Roy M, Bandyopadhyay A, Bose S. Laser surface modification of electrophoretically deposited hydroxyapatite coating on titanium. *J Am Ceram Soc* 2008;**91**:3517–21.
25. Roy M, Bandyopadhyay A, Bose S. In vitro antimicrobial and biological properties of laser assisted tricalcium phosphate coating on titanium for load bearing implant. *Mater Sci Eng C* 2009;**29**:1965–8.

26. Comesaña R, Quintero F, Lusquiños F, Pascual MJ, Boutinguiza M, Durán A, et al. Laser cladding of bioactive glass coatings. *Acta Biomater* 2010;**6**(3):953–61.
27. ISO 13779-3:2008. Implants for surgery – hydroxyapatite. Part 3. Chemical analysis and characterization of crystallinity and phase purity.
28. Gross KA, Berndt CC, Herman H. Amorphous phase formation in plasma-sprayed hydroxyapatite coatings. *J Biomed Mater Res* 1998;**39**:407–14.
29. Gross KA, Berndt CC, Stephens P, Dinnebier R. Oxyapatite in hydroxyapatite coatings. *J Mater Sci* 1998;**33**:3985–91.
30. Penel G, Leroy G, Rey C, Bres E. MicroRaman spectral study of the PO_4 and CO_3 vibrational modes in synthetic and biological apatites. *Calcif Tissue Int* 1998;**63**:475–81.
31. Posset U, Löcklin E, Thull R, Kieferm W. Vibrational spectroscopic study of tetracalcium phosphate in pure polycrystalline form as a constituent of a self-setting bone cement. *J Biomed Mater Res* 1998;**40**:640–5.
32. Kim H, Camata RP, Vohra YK, Lacefield WR. Control of phase composition in hydroxyapatite/tetracalcium phosphate biphasic thin coatings for biomedical applications. *J Mater Sci Mater Med* 2005;**16**(10):961–6.
33. De Groot K, Klein CAPT, Wolke JG, De Blieck-Hogervorst. Chemistry of calcium phosphate bioceramics. In: Yamamuro T, Hench LL, Wilson J, editors. *Handbook of bioactive ceramics*, vol. II. Boca Ratón: CRC Press; 1990.
34. Cihlar J, Buchal A, Trunec M. Kinetics of thermal decomposition of hydroxyapatite bioceramics. *J Mater Sci* 1999;**34**:6121–31.
35. Liao CJ, Lin FH, Chen KS, Sun JS. Thermal decomposition and reconstitution of hydroxyapatite in air atmosphere. *Biomaterials* 1999;**20**:1807–13.
36. Zhou J, Zhang X, Chen J, Zeng S, DeGroot K. High temperature characteristics of synthetic hydroxyapatite. *J Mater Sci: Mater Med* 1993;**4**:83–5.
37. Chen J, Tong W, Cao Y, Feng J, Zhan X. Effect of atmosphere on phase transformation in plasma-sprayed hydroxyapatite coatings during heat treatment. *J Biomed Mater Res* 1997;**34**:15–20.
38. Ducheyne P, Qiu Q. Bioactive ceramics: the effect of surface reactivity on bone formation and bone cell function. *Biomaterials* 1999;**20**: 2287–303.
39. DeBruijn JD, Flach TS, Leenders HA, van de Brink J, van Blitterswijk AC. Degradation and interface characteristics of plasma sprayed hydroxyapatite coatings with different crystallinities. In: *Bioceramics, vol. 5.* Kyoto: Kobushi Kankokai; 1992. pp. 291–8.
40. Maxian SH, Zawadski JP, Dunn MG. In vitro evaluation of amorphous calcium-phosphate and poorly crystallized hydroxyapatite coating on titanium implants. *J Biomed Mater Res* 1993;**27**:111–7.
41. Driessens FCM. Formation and stability of calcium phosphate in relation to the phase composition of the mineral in calcified tissues. In: De Groot K, editor. *Bioceramics of calcium-phosphate*. Boca Ratón: CRC Press; 1983.
42. Dorozhkin SV. Bioceramics of calcium orthophosphates. *Biomaterials* 2010;**31**:1465–85.
43. Ehara A, Ogata K, Imazato S, Ebisu S, Nakano T, Umakoshi Y. Effects of α-TCP and TetCP on MC3T3-E1 proliferation, differentiation and mineralization. *Biomaterials* 2003;**24**:831–6.
44. Constantino PD, Friedman CD, Jones K, Chow LC, Sisson GA. Experimental hydroxyapatite cement cranioplasty. *Plast Reconstr Surg* 1992;**90**:174–91.
45. Wiltfang J, Merten HA, Schlegel KA, Schultze-Mosgau S, Kloss FR, Rupprecht S, et al. Degradation characteristics of α and β tri-calcium-phosphate (TCP) in minipigs. *J Biomed Mater Res* 2002;**63**:115–21.
46. Driessens FCM, DeMayer E, Fernández E, Boltong MG, Berger G, Verbeeck RMH, et al. Amorphous calcium phosphate cements and their transformation into calcium deficient hydroxyapatite. *Bioceramics* 1996;**9**:231–4.
47. Kokubo T, Matsushita T, Takadama H, Kizuki T. Development of bioactive materials based on surface chemistry. *J Eur Ceram Soc* 2009;**29**: 1267–74.